Feedback Control of a Shear Layer for Aero-Optic Applications

Casey Fagley, Jürgen Seidel, Thomas McLaughlin
Department of Aeronautics, U.S. Air Force Academy, Colorado Springs, CO 80840, USA

February 15, 2011

Abstract
High fidelity, low dimensional model and control development for complex flow fields is a challenging yet highly rewarding research topic. The systematic modeling and control approach developed in this paper is applied to suppress optical distortions caused by large scale density variations in a free, unstable shear layer behind a backward facing step. Simulations of an unforced and open-loop forced shear layer, based on the compressible Navier-Stokes equations, are used to compile a flow state database to formulate a linear basis set using proper orthogonal decomposition. It is shown that nonlinear auto regressive exogenous models accurately predict the fundamental behavior and forcing interaction of the POD time coefficients. This low dimensional model allows for simulation of open and closed loop dynamics, prediction of future flow states, and is ultimately utilized to develop feedback control algorithms. Feedback results using nonlinear, adaptive regulation of the vortex shedding phenomenon indicate that a 35 per cent reduction in the optical aberrations is achieved.

1. INTRODUCTION

The performance of airborne optical systems is severely hampered by beam distortions due to the unsteady density variations in the air flow over the optical aperture, especially when looking back (11, 18). These density variations ($\rho(x,t)$) translate into optical beam distortions via the index-of-refraction ($n(x,t)$),

$$n(x,t) = K_{GD}\rho(x,t), \tag{1}$$

where K_{GD} is the Gladstone-Dale constant. The optical path length is consequently affected by the varying index of refraction through the shear layer as in,

$$OPL = \int_0^l n(\xi,t)d\xi. \tag{2}$$

An initially collimated wave front that passes through a variable density field will be distorted by the spatial and temporal variations, resulting in reduced focus and beam intensity in the far field. These distortions away from the ideal diffraction limit can greatly reduce the usefulness of an airborne optical system. For convenience, the wave front distortions are typically expressed as the optical path difference,

$$OPD(x,z,t;y) = OPL(x,z,t;y) - \overline{OPL(x,z,t;y)}^{x,z}, \tag{3}$$

where it is assumed that the beam extends in the y-direction and the overbar denotes the average over the aperture.

Numerous experiments by Jumper and his coworkers investigated many aspects of these aero-optical flow fields, ranging from free shear layers to an idealized, two-dimensional turret and a three-dimensional turret (9, 11, 12, 17, 18, 23, 29, 30, 31, 36, 42). The free shear layer forming behind such a turret, due to its natural instability, forms large, almost periodic structures. These structures are the source of density variations and therefore optical aberrations. Jumper and his coworkers investigated the performance of a variety of vortex generating devices and found significant changes in the optical distortions of a beam propagating through the shear layer. While these passive flow control devices have a beneficial effect on the flow field in terms of the predictability of the optical aberrations, changing flow conditions (e.g. flow velocity) cannot be addressed with these devices. Feedback flow control provides a promising extension to passive control that can take these variations of the flow parameters into account by instantaneously sensing the flow state and adapting and actuating the flow. The goal of feedback flow control is to provide a method to modify the flow field such that the most optically detrimental coherent structures are mitigated over a range of flow conditions. Due to the close coupling of the density field and the index-of-refraction, the density field is analyzed directly, keeping in mind that the optical aberrations are linearly dependent on the path integral of the density field and hence successfully controlling the density fluctuations will also mitigate the optical distortions.

Feedback flow control design strategies can be divided into two main categories: those that use a model and model free approaches. The model free approach utilizes adaptive control techniques to feedback global flow variables. Adaptive control varies open loop parameters to produce desirable effects in the flowfield. Typically the model free approach is used in an experimental setting because a large amount of time is necessary for control adaptation (3). Control laws such as adaptive extremum seeking controllers have been shown to suppress combustion instabilities by varying the phase of an open loop acoustic signal (20, 22). Similarly this adaptive method has been used to control the flow separation on a NACA4412 airfoil with a flap to achieve increased lift at high angles of attack (3). It could be argued that the model free approach is less likely to reach desired performance margin and control goals; however, it is relatively simple to implement.

Alternative methods entail using reduced order modeling procedures to formulate low dimension numerical models for controller development. Model flow control techniques do vary in the amount of retained fluid dynamics inherent in the model. For example black box models which are trained online or offline relate input/output dynamics of an experiment or computation. Williams et al. (41) used the prediction error method to identify a first order state space model to increase lift on a semi-circular wing. A PID controller designed for the trained model showed desirable gust alleviation on a three dimensional wing. A step up in retained fluid dynamics in modeling approach is the Galerkin model. A truncated Proper Orthogonal Decomposition (POD) spatial mode set is projected onto the Navier Stokes equations, resulting in a set of quadratic ordinary differential equations (4, 14, 25, 33, 37). Due to the truncation of the mode set the resulting equations are mathematically unstable because of the unsatisfied boundary conditions (28). Also, the actuation is added through the body force term of the Navier-Stokes which is linearly superimposed at a given location in the flow field. Nonetheless, Galerkin models provide insight into the flow physics and basic controller design. Noack et al. (24) and Ahuja et al. (1) have addressed the mathematical stability issue of the Galerkin model and successfully controlled a three dimensional cylinder wake and a two-dimensional wake behind an inclined flat plate, respectively.

The focus of the current research is to design adaptive control algorithms based on reduced order models (ROMs). Figure 1 shows an overview of the feedback flow control design approach. The control design approach taken in this work relies heavily on the multidisciplinary combination of current methodologies in computational fluid dynamics as well as control theory. As shown in Figure 1, a database of flow states is first compiled from the results of unforced as well as open-loop forced simulations. For the open-loop simulations, the disturbances are introduced by periodic blowing and suction slots at critical geometrical locations. The frequency and amplitude of the forcing signal are varied to probe the flow response throughout a given forcing parameter space. The resulting forced and unforced flow state database is numerically reduced using POD, which yields an optimal linear representation of the flow over the forcing parameter range. The computed POD spatial modes and time coefficients are then scrutinized further for controller development as well as flow state estimation.

POD modes and their adjoint amplitudes for a forcing scenario provide important information about the interaction of the forcing input with the flow field. These interactions are modeled through the time coefficients using system identification techniques. The reduced order model developed purely from open loop and unforced flow information is shown to accurately simulate closed loop behavior as well as predict off-design flow scenarios. An adaptive feedback regulator is applied to the reduced order model to suppress density abberations present in the shear layer. As seen in Figure 1 each step in the design process provides for the possibility of iterative adjustments of parameters to increase model and controller performance (paths 1 through 4). The individual blocks in this flowchart will be described in

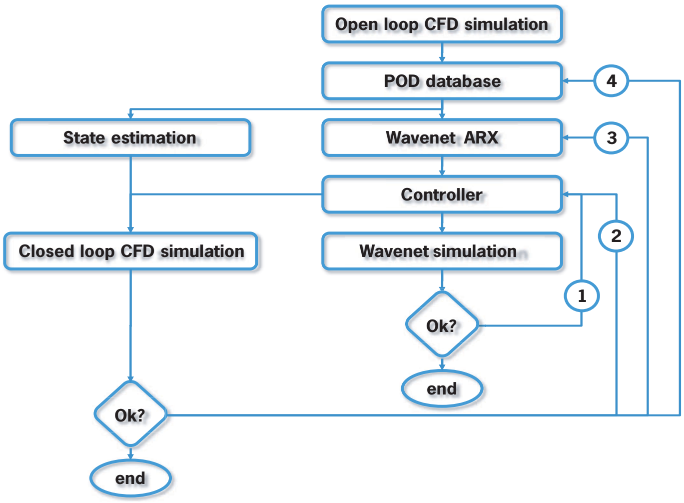

Figure 1: Flowchart of the feedback control development process.

the following sections as a feedback control law is designed for the flow over a backward facing step.

2. OPEN-LOOP SIMULATIONS

The framework of this control design approach is based upon the use of open-loop numeric simulations. The simulations were performed using COBALT from Cobalt Solutions, LLC, a commercial unstructured finite-volume code developed for the solution of the compressible Navier-Stokes equations. The basic algorithm is described in (40), although substantial improvements have been subsequently made. The numerical method is a cell-centered finite volume approach applicable to arbitrary cell topologies (e.g, hexahedra, prisms, tetra-hedra). The spatial operator uses the exact Riemann Solver of (15), least squares gradient calculations using QR factorization to provide second order accuracy in space, and TVD flux limiters to limit extremes at cell faces. A point implicit method using analytic first-order Jacobians is used for advancement of the discretized system. For time-accurate computations, a second order accurate method with Newton sub-iterations is employed. For parallel performance, COBALT utilizes the domain decomposition library ParMETIS (19) to provide optimal load balancing with a minimal surface interface between zones. Communication between processors is achieved using Message Passing Interface (MPI), with parallel efficiencies above 95% on as many as 1024 processors (16). For turbulent simulations, numerous turbulence models are available in COBALT. For the current investigation, since the unsteady motion of the large coherent structures in the flow is of paramount interest, Delayed Detached Eddy Simulations (DDES) were performed (39).

The geometry under investigation is a backward facing step with a step height of $H = 0.15$ m, and a ramp length $L_R = 0.85$ m. This geometry was chosen to be consistent with an experimental model used and tested in a subsonic wind tunnel. The domain length was $L_x = 4$ m downstream of the step.

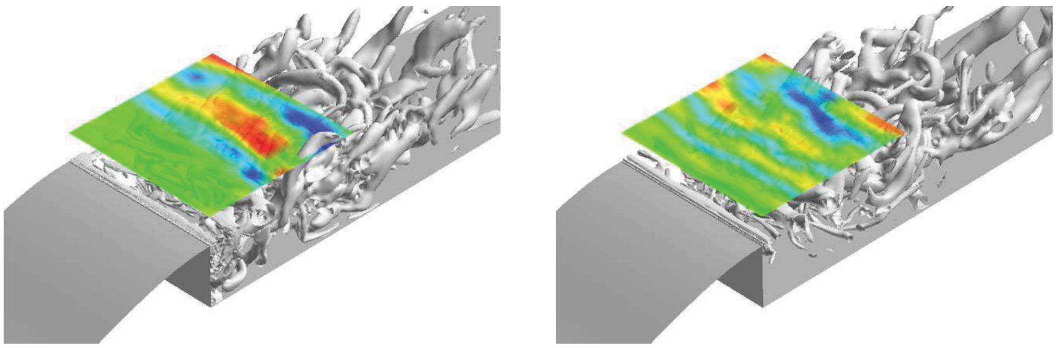

(a) $F_f = 400$Hz, $A/U_\infty = 0.1$ (b) $F_f = 800$Hz, $A/U_\infty = 0.1$

Figure 2: Instantaneous isosurface of flow structures and associated OPD for various forcing conditions.

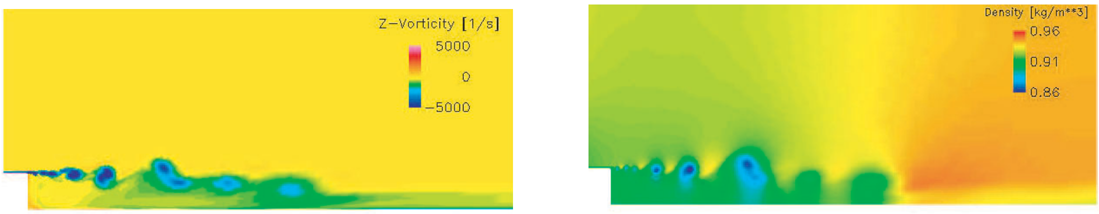

(a) Spanwise vorticity. (b) Density.

Figure 3: Instantaneous distribution of spanwise vorticity and density in a two-dimensional simulation.

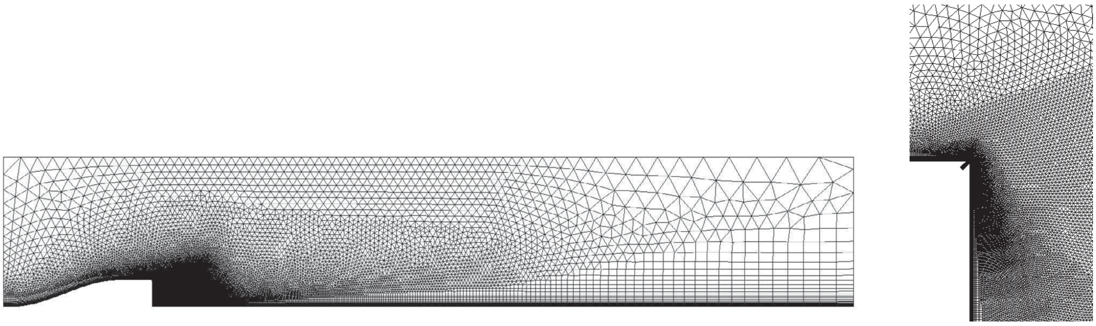

(a) 2D Grid (b) B/S slot

Figure 4: a)Two-dimensional CFD grid. b) Grid at the step showing the blowing/suction slot.

The modeled wind tunnel height is $L_y = 0.8$ m. Initial three dimensional simulations (34) showed that the OPD is directly affected by the large, spanwise, coherent structures as seen in Figure 2. In addition, the OPD data corroborate that the structures which cause the largest optical aberrations are nearly two-dimensional. Figure 3 shows results from an unforced simulation in two-dimensions. The simulations show shear layer structures very similar to the ones observed in the three-dimensional simulations as well as some of the nonlinear dynamics such as vortex pairing. For this reason a two-dimensional simulation and modeling approach is chosen to investigate feedback control of the OPD.

The flow conditions were defined by the inflow Mach number Ma = 0.3 and sea level standard atmospheric conditions. The Reynolds number based on the step height was $\mathrm{Re} = 10^6$; these flow parameters resulted in a Reynolds number of $\mathrm{Re}_\theta \approx 4500$ based on the momentum thickness of the separating boundary layer; the time step was chosen as $\Delta t = 10^{-6}$s to capture the resolved turbulent time scales.

Figure 4 shows the two-dimensional grid. The grid spacing at the step was defined to be $\Delta x = 0.1$ mm. This grid contains approximately 58,000 nodes and 90,000 elements. Grid clustering was used on the bottom wall and in the region of interest in the free shear layer. To build a database of flow states that would be used to define the reduced order model for the flow field, unforced simulations were performed first. In a second step, open-loop active flow control (AFC), which in the simulations was implemented using an externally controlled blowing/suction boundary condition (Figure 4(b)), was studied and the data was added to the development cycle of the database. These forcing cases were particularly valuable for describing the transient flow features present during the initial development of the open-loop forced shear layer as well as the vortex pairing that occurred when forcing was initiated. The results from the simulations provided a comprehensive database of the free shear layer, which was used to develop feedback control strategies as well as to compare the effectiveness of feedback control applied to the aero-optics problem. The magnified view of the step edge is shown in Figure 4(b) which shows the blowing/suction slot at the trailing edge of the step at an angle of 45°. The boundary layer grid spacing was chosen such that the final y^+ value at the step was $y^+ \simeq 1$.

From the unforced data it was determined that the vortical structures in the shear layers naturally occur at a frequency, $F_n \simeq 400$Hz at a downstream distance, $x/H = 2$. For the open-loop forcing cases, only periodic inputs with varying frequency and amplitude were considered. The range of forcing parameters was chosen by perturbations to the natural shedding frequency of the flow at a range of experimentally achievable actuation limits. The blowing and suction actuation frequency ranged from $F_f = 400$Hz to $F_f =$

Table 1: Summary of computed forcing cases.

	400Hz	600Hz	800Hz	1000Hz
$A/U_\infty = 0.3$	x	x	x	x
$A/U_\infty = 0.2$	x	x	x	x
$A/U_\infty = 0.1$	x	x	x	x
$A/U_\infty = 0.05$	x	x	x	x
$A/U_\infty = 0.01$	x	x	x	x

1000Hz and the amplitude between $A/U_\infty = 0.01$ and $A/U_\infty = 0.3$, where U_∞ is the freestream velocity and A is the velocity through the blowing/suction slot, resulting in the time dependent blowing and suction velocity $u_f(t) = A\sin(2\pi F_f t)$. A summary of all the computed cases is given in Table 1.

3. REDUCED ORDER MODEL

3.1. Numerical Reduction

The simulations in Section 2 provide a database of flow states over the forced and unforced parameter range. The flow solution database is denoted by $\Omega \in \mathbb{R}^{n_t \times n_x}$ where n_x is the number of spatial locations (typically on the order of 10^6) and n_t is the total number of time steps (typically on the order of 10^3). This database is governed by the compressible Navier Stokes equations,

$$\dot{\Omega}(\mathbf{x},t,\mathbf{u}) = f(\mathbf{x},t,\mathbf{u}), \tag{4}$$

where $\mathbf{x}$ is a vector spanning the finite dimensional state space, time ($0 < t < t_f$), input (u) and $f()$ is a time variant, nonlinear function. The dataset Ω is of very high order and it is not feasible to work with this data directly for controller design. A linear basis representation by means of proper orthogonal decomposition (POD), also known as the Karhunen-Loeve process or principal component analysis, has been widely accepted as an appropriate scheme to reduce the dimensionality of the dataset and extract pertinent flow features (4). In particular, the method of snapshots (38) allows for efficient decomposition into spatial modes and time coefficients. The eigenvalues and eigenvectors of the spatial correlation matrix give the linear basis representation. Mathematically this operation is analogous to the singular value decomposition

$$\Omega(\mathbf{x},t,\mathbf{u}) = U\Sigma V^*, \tag{5}$$

where U is an orthonormal matrix with dimension $n_x \times n_x$, V^* is also an orthonormal matrix with dimension $n_t \times n_t$, Σ is a diagonal $n_x \times n_t$ matrix in which the n_t (because typically $n_t < n_x$) singular values are arranged in decreasing magnitude on the diagonal. The singular values of Ω are also the eigenvalues of $\Omega^T\Omega$. Next, define $Q \equiv U\Sigma$ in Equation 5, which yields $\Omega = QV^*$. This can be written in summation form, as shown in Equation 6, such that q_i is the i^{th} column of Q; likewise, v_i is the i^{th} column of V,

$$\Omega(\mathbf{x},t,\mathbf{u}) = \sum_{i=1}^{m} q_i v_i^*. \tag{6}$$

Equation 6 is still an identity, i.e. no approximations have been introduced. In Equation 6 the i^{th} temporal coefficient, $a^i(t)$, is exactly equivalent to the i^{th} column of Q. Likewise, the i^{th} spatial mode, $\varphi_i(x,y)$, is represented by the i^{th} row vector of V^*. The system Ω can then be written as $\Omega = \sum_{i=1}^{m} a_i(t)\varphi_i(\mathbf{x})$. To reduce the order of this system, $m' < m$ is chosen and the decomposition becomes

$$\Omega(\mathbf{x},t,\mathbf{u}) \simeq \sum_{i=1}^{m'} a_i(t,\mathbf{u})\varphi_i(\mathbf{x}\,|\,\mathbf{u}). \tag{7}$$

where now the right hand side is an approximation of Ω. Because the singular values are related to the POD mode energy and are ordered by magnitude ($\sigma_1 > \sigma_2 > \cdots > \sigma_n$), the dominant spatial and temporal modes appear first in the matrices U and V, respectively.

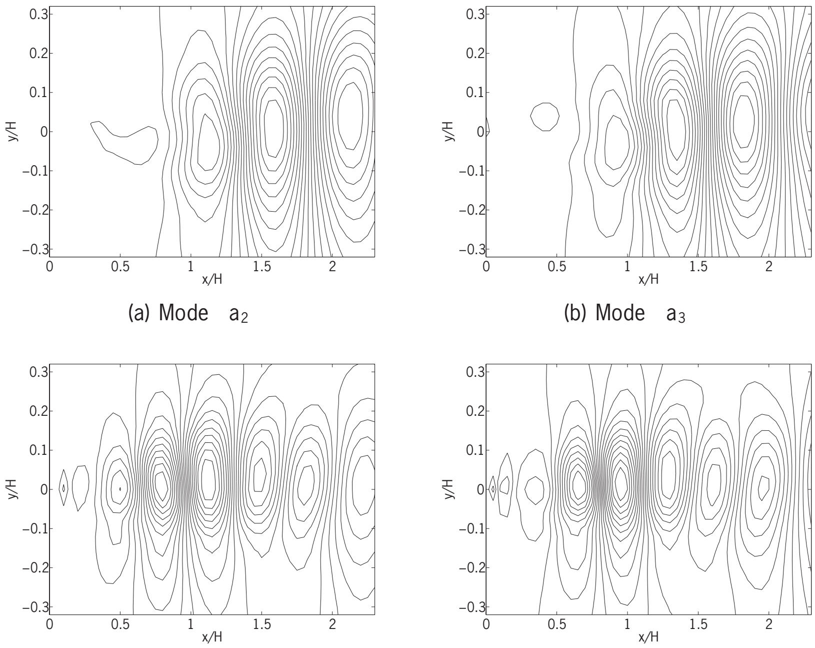

(a) Mode a_2 (b) Mode a_3

(c) Mode a_4 (d) Mode a_5

Figure 5: Four spatial mode set φ_i computed by method of snapshots. As seen modes a_2 and a_3 show a larger wavelength than modes a_4 and a_5. Note: Mean flow (a_1) was subtracted before POD process.

The above decomposition is a valid approximation for large, coherent structures prevalent in periodic flow fields. While many flavors of POD exist, all methods hinge on the eigen-solution of the spatial correlations in time, but effectively differ by mode organization (sorting) and truncation method. For example, traditional POD modes are organized by singular value magnitude (or energy content) and the truncation location is determined by an acceptable energy content in the retained modes. In contrast, balanced POD (BPOD, (32)) organizes modes based on the controllability and observability gramians and truncation is determined by scrutinizing Hankel values of these gramians.

The added complexity in determining an appropriate POD method for the purpose of feedback flow control design is in capturing the interaction between the forcing input and the flow response within the truncated mode set. During an open-loop forced simulation the flow undergoes some transient development, which results in the spatial modes ($\varphi_i(\mathbf{x})$) evolving over time. To capture this slow transient development, Siegel et al. (35) devised a strategy called Double Proper Orthogonal Decomposition (DPOD) to model the forced wake behind a circular cylinder. In DPOD, POD is used first to capture the almost periodic flow behavior and a second time to quantify the slow transients of the spatial modes. The second decomposition represents the spatial mode fluctuations over time which can capture forcing-flow interaction. The DPOD decomposition is written as $\Omega = \sum_{i=1}^{m'} \sum_{j=1}^{n'} a_{ij}(t)\varphi_{ij}(\mathbf{x})$.

These POD methods as well as various spatial domains, datasets in frequency/amplitude parameter space, and time steps were studied to determine an appropriate mode set for the shear layer behind the backward facing step. In the end, while BPOD and DPOD showed marginal improvements in the model for certain cases, the traditional method of snapshots and truncation via energy content were used to compute the linear basis representation seen in Figure 5.

The spatial modes shown in Figure 5 represent the large coherent structures of the Kelvin-Helmholtz vortices. The spatial domain focused on the shear layer and therefore the four mode representation does neglect higher order turbulent effects apparent in the recirculation zone. However, since the OPD is most affected by the flow structures with the largest density variations, this selection was deemed appropriate for the investigation of mitigation strategies for optical distortions due to a free shear layer. Figure 6 shows the temporal behavior of the first 2 pairs of fluctuating spatial modes. As shown for the forcing case of $f = 600$Hz, $A/U_\infty = 0.1$ (see Table 1), the flow responds very nonlinearly to the forcing as evidenced by the temporal coefficients. The start up transient is apparent between $0\text{s} \leq t \leq 0.13\text{s}$ and the ending transient from $0.25\text{s} \leq t \leq 0.33\text{s}$ in all four modes. The nonlinear periodic behavior of

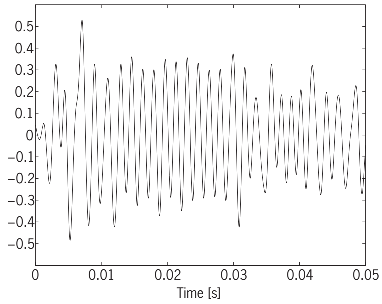

(a) Mode a_2

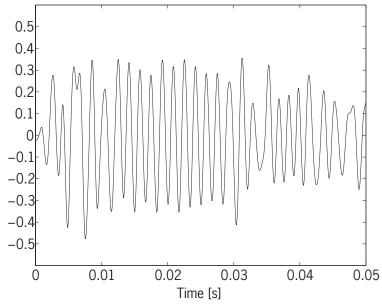

(b) Mode a_3

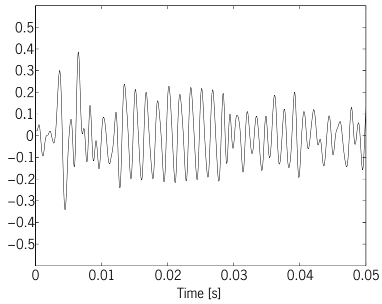

(c) Mode a_4

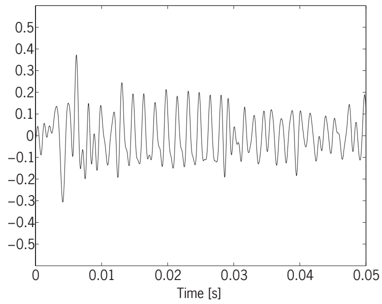

(d) Mode a_5

Figure 6: POD mode amplitudes (a_i) of mode set for off design simulation case $f = 600Hz$, $A/U_\infty =$

the temporal coefficients represents the state of the flow field; in combination with the spatial modes, the large coherent structures of the shear layer can be represented by the four mode reduced order model.

3.2. System Identification

Nonlinear, autoregressive exogenous (NL-ARX) system identification techniques are implemented to model the behavior of the POD time coefficients over a range of unforced and open-looped forced flow state dynamics. A state space representation of the flow field is given by

$$\Omega(\mathbf{x},t,\mathbf{u}) = f(\mathbf{x},t,\mathbf{u}) \simeq \sum_{i=1}^{m'}(t,\mathbf{u})\varphi_i(\mathbf{x}\,|\,\mathbf{u}), \tag{8}$$

where $x \in \mathbb{R}^{n_x}$, $t_o \leq t \leq t_1$, and $\mathbf{u}(t|F,A) = A\sin(2\pi Ft)$. Eqn. 8 provides the basis for applying system identification tools. To understand the time evolved behavior of the mode amplitudes the derivative in time must be computed,

$$\dot{\Omega}(\mathbf{x},t,\mathbf{u}) \simeq \sum_{i=1}^{m'}[\dot{a}_i(t,\mathbf{u})\varphi_i(\mathbf{x}\,|\,\mathbf{u}) + a_i(t,\mathbf{u})\dot{\varphi}_i(\mathbf{x}\,|\,\mathbf{u})]. \tag{9}$$

The second term, $a_i(t, \mathbf{u})\dot{\varphi}_1(\mathbf{x}|\mathbf{u})$, vanishes since φ is time invariant, so all of the nonlinearities of the system are contained within the evolution of the mode amplitudes $\dot{a}_i(t|\mathbf{u})$. The system is represented in state space form as

$$\begin{cases} \dot{a}(t,u) = G(a(t,\mathbf{u})) \\ \Omega(\mathbf{x},t) \simeq \varphi(\mathbf{x}\,|\,\mathbf{u})a(t,\mathbf{u}) = \varphi(\mathbf{x}\,|\,\mathbf{u})L(\mathbf{x_s}) \end{cases} \tag{10}$$

where $G(a(t, \mathbf{u}))$ and $L(\mathbf{x}_s)$ are unknown, nonlinear functions. Referring to Figure 1, the control design approach splits into two separate paths. One is the formulation of a reduced order model, $a(t, u) = G(a(t, \mathbf{u}))$, and the other is the development of surface based flow state estimators, $\hat{a}(t, \mathbf{u}) = \varphi(\mathrm{x}|\mathbf{u})L(\mathbf{x}_s)$. Both model and state estimator are necessary for a feedback control simulation.

A mathematical model which represents the time coefficients of the numeric approximation over the open-loop forcing parameter space, $u(t|F,A)$, needs to be developed. NL-ARX system identification techniques allow for prediction and simulation of the POD mode amplitudes. NL-ARX models are not limited to single-input single-output systems. NL-ARX are strictly causal systems, depending on current and past time histories of chosen inputs. For the development of a NL-ARX model, a regression vector is formed such that the previously simulated mode amplitudes and current and past actuation inputs are compiled in a vector,

$$\theta(t) \equiv [u(t)\ldots u(t-n_u), a_1(t-1)\ldots a_1(t-n_{a_1})\ldots a_i(t-1),\ldots a_i(t-n_{a_i})]. \tag{11}$$

This regression vector, $\theta(t)$, serves as the input to the low dimensional NL-ARX model. A nonlinear function, G, relates the regression vector to the time coefficient at the future time $k+1$, such that $\hat{a}_{k+1} = G(\theta(k))$. Typically, G is developed using Hammerstein-Wiener methods, Volterra kernels, neural network models, etc. Once a model structure is chosen, the simulation or prediction error is minimized over a training data set in a least squares sense.

Previous feedback flow control work of the authors used artificial neural network autoregressive exogenous (ANN-ARX) systems to identify the dynamic behavior of the time coefficients in the forced cylinder wake (7, 8, 35). This nonlinear system identification technique has been argued to be a universal approximator, capable of representing any type of data trend (26). However, some inherent problems of ANN models exist. First, there is no straightforward method for designing the network, including determining the number of hidden neurons, the number of layers, or the parameters of the regression vector. Furthermore, training relies heavily on trial and error to find a combination of parameters that yields acceptable results. Second, the convergence of these networks depends strongly upon the initial (usually random) weights in the weighting matrices. This can lead to drastically different results when training a single network with different sets of parameters. Third, a properly trained network will behave as a *black box* from which little mathematical and physical insight can be gained. And finally, training times are extremely long due to multimodal error surfaces which tend to trap the solution in local minima. This also contributes to the vastly different network parameters obtained from the random initial network weights.

A powerful basis function for non-linear model development is a wavelet; they are known for their ability to compress, decompose, and approximate scientific data sets accurately and efficiently. Wavelet basis functions are used in many technical fields including image processing, edge detection, large scale monitoring processes, transient detection, etc. Mathematically, the *mother wavelet,* Ψ, can be written as

$$\Psi(t)_{u,s} = \Psi\left(\frac{t-u}{s}\right), \tag{12}$$

where u denotes the shift or translation and s the dilation or frequency content of the wavelet basis function. In the current modeling approach, wavelets were used as transfer functions to create a WaveNet (WN). These wavenets were first introduced by Zhang et al. and have been applied to many areas such as functional approximation, system identification, adaptive control, and nonlinear modeling and optimization (5, 21, 43, 44). The WN is typically initialized using a dyadic wavelet decomposition (27). Multiple techniques exist to design the architecture of such wavenets. One technique employs the wavenet as a preprocessing filter for the nonlinear ANN identifier. An example of this type of network is the identification of transients in power signals (2). Another approach is to replace the existing transfer function of a neural network (usually sigmoid or signum functions) with a radial basis function. This approach was taken in the current work to design and train wavenets for feedback flow control applications. The fundamental WN structure used to model the system in given in Equation 13,

$$\hat{a}_j(t_k \mid \Theta_j) = (\Theta_j - r)PL + \sum_{i=1}^{n} a_{si}\Psi_s(b_{si}(\Theta_j - r)Q - c_{si}) + \sum_{i=1}^{n} a_{wi}\Psi_w(b_{wi}(\Theta_j - r)Q - c_{wi}) + d \tag{13}$$

where r is the mean of the regression vector, P is the linear subspace, L are the linear weights, Q is the nonlinear subspace, a_{s_i} are the scaling block coefficients, b_{s_i} are the scaling block dilations, c_{s_i} are the scaling block translations, a_{w_i} are the wavelet block coefficients, b_{w_i} are the wavelet block dilations, c_{w_i} are the wavelet block translations.

Moreover, $\Psi_s(x)$ is the scaling function. Here, the scaling function was chosen to be a class of radial basis functions such that

$$\Psi_s(x) = e^{-\frac{1}{2}\|x\|_2^2} \ni f{:}\mathbb{R}^n \to \mathbb{R}. \tag{14}$$

Likewise, $\Psi_w(x)$ is the wavelet basis, which is also a radial basis function in the form

$$\Psi_w(x) = (\| x \|_0 - \| x \|_2^2)e^{-\frac{1}{2}\|x\|_2^2} \ni g{:}\mathbb{R}^n \to \mathbb{R}. \tag{15}$$

The linear and nonlinear subspace matrices (P and Q, respectively, in Equation 13) are initialized by a principal component analysis based on an optimal representation of the system linearities in the linear block as well as the nonlinear block. Given a set of initial parameters for the WN, the model is simulated and the global error of the training data is determined as $a_j(t)–\hat{a}_j(t)$. The parameters of the WN are subsequently updated via a gradient descent method to minimize the cost function $J_\theta = \|\hat{f}(t) - f(t)\|^2$.

Just as with POD data selection, NL-ARX requires data selection, i.e. the selection of forcing cases, for model development. A total of 12 open-loop cases, all of which contained starting and ending transients from the unforced flow state and back to it, were computed to understand the influence of actuation with varying frequency and amplitude on the flow. The results showed that the time coefficients reacted almost linearly to the blowing and suction amplitude, i.e. the response of the mode amplitudes, $a_j(t)$, scaled linearly with amplitude input. In contrast, the flow response was highly nonlinear with respect to the forcing frequency. Thus, the three training data sets highlighted in Table 2 were chosen to provide a basis for the WNARX model. The case $F_f/F_n = 1$, $A/U_\infty = 0.10$ was chosen to be the validation case for the model.

Table 2: Summary of cases. x: POD database, ✓: WN training cases, o: validation case.

	400Hz	**600Hz**	**800Hz**
$A/U_\infty = 0.1$	✓	o	✓
$A/U_\infty = 0.05$	x	✓	x
$A/U_\infty = 0.025$	x	x	x
$A/U_\infty = 0.0125$	x	x	x

The WN model has four outputs which are the estimated mode amplitudes. The inputs are formed by the regression vector in (11). A regression vector is selected for each simulated output of the model. The structure of this vector is chosen by coupling mode interaction and external input. A summary of final parameters for the dynamic model is presented in Table 3. As shown, modes 1 and 2 are coupled, but decoupled from modes 3 and 4. The coupling of these mode pairs is due to the traveling wave character of the structures in the flow, which can be represented by two modes and their time coefficients that are shifted in space and time, respectively.

Table 3: Summary of parameters chosen for the WNARX model.

Mode a_i	**Wavelets**		**Regressors**			
	$\boldsymbol{a_1}$	$\boldsymbol{a_2}$	$\boldsymbol{a_3}$	$\boldsymbol{a_4}$	**u**	
a_1	2	4	1	0	0	1
a_2	21	1	5	0	0	1
a_3	10	0	0	4	2	2
a_4	16	0	0	2	4	2

The WNARX model was validated for an off design flow case for which the forcing signal was turned on at simulation time $t = 0$s, at which point the flow goes through a transient before locking into the forcing frequency. The forcing was then turned off at $t = 0.025$s (corresponding to 15 forcing periods)

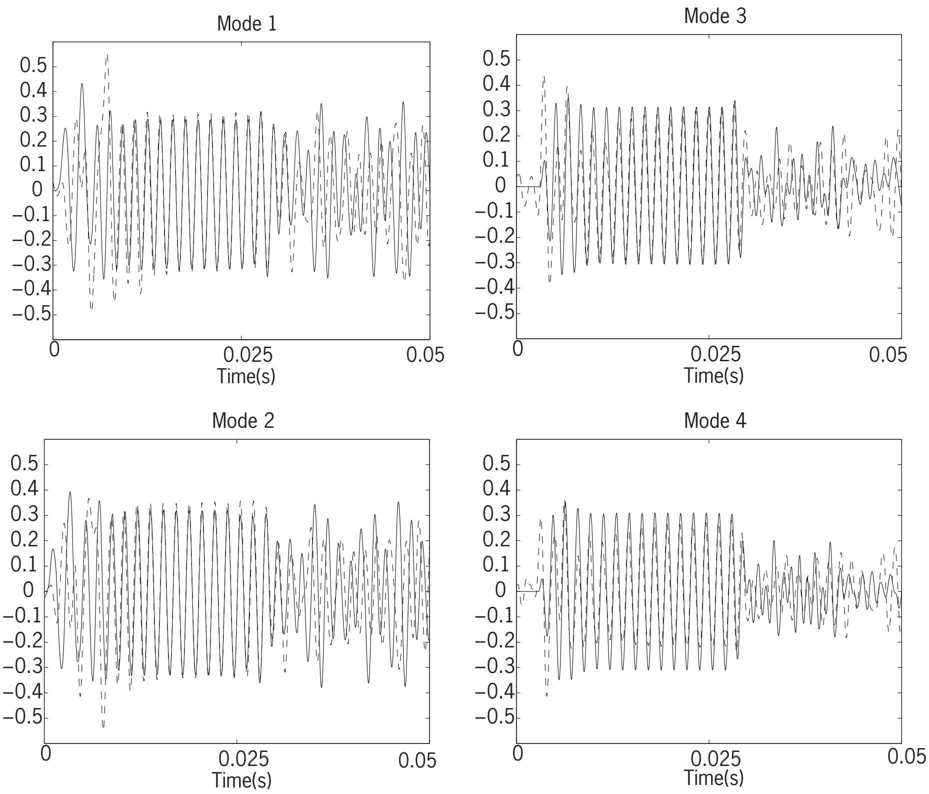

Figure 7: Off design validation of the four mode WNARX model for flow case of F_f = 600Hz and A/U_∞ = 0.1. WNARX output (–), POD model (– –).

to reestablish the unforced flow state. As shown in Figure 7, the model captures the lock-in region ($0.01s < t < 0.03s$) of the periodic forcing very well. Once the forcing was turned off at $t = 0.025s$, the model accurately predicted the type of nonlinear signal in the unforced flow. Expecting an exact replication of the transients and the unforced time coefficients is unrealistic since the signal was extremely nonperiodic. However, it is important to note that the model of the unforced flow does not decay to zero over time. This indicates that there is a periodic attractor to the nonlinear function for the WNARX system. The similarities in periodic trends furthermore suggest that the attractor is near the solution of the unforced state.

4. FEEDBACK CONTROL

4.1. Adaptive Regulation of Model Simulation

Developing the components for a closed-loop simulation is a multi-step iterative process as shown in Figure 1. The model developed in Section 3 provides accurate predictions of mode amplitudes encompassing unforced and forced flow states within a forcing frequency and amplitude parameter range. However, it remains to be seen if the model is capable of adequately simulating the highly nonlinear dynamics expected for the closed-loop case. To close the loop a non-linear adaptive regulation feedback scheme is chosen. Adaptive control minimizes the number of simulations needed to precondition fixed gain control methods. Also adaptivity allows for compensation of model/CFD uncertainties. The equations describing this variation of direct adaptive control are,

$$\begin{aligned} U &= G_e e_y \\ \dot{G}_e &= -e_y e_y^T \gamma_e, \end{aligned} \tag{16}$$

where G_e is the adaptive gain matrix, γ_e is the adaptability weight, and e_y is the error between output and desired reference signal, $e_y = \hat{a} - a_{ref}$.

For multi-input multi-output (MIMO) systems, e_y and γ_e are matrices of size $n_{out} \times n_{in}$. Also, the

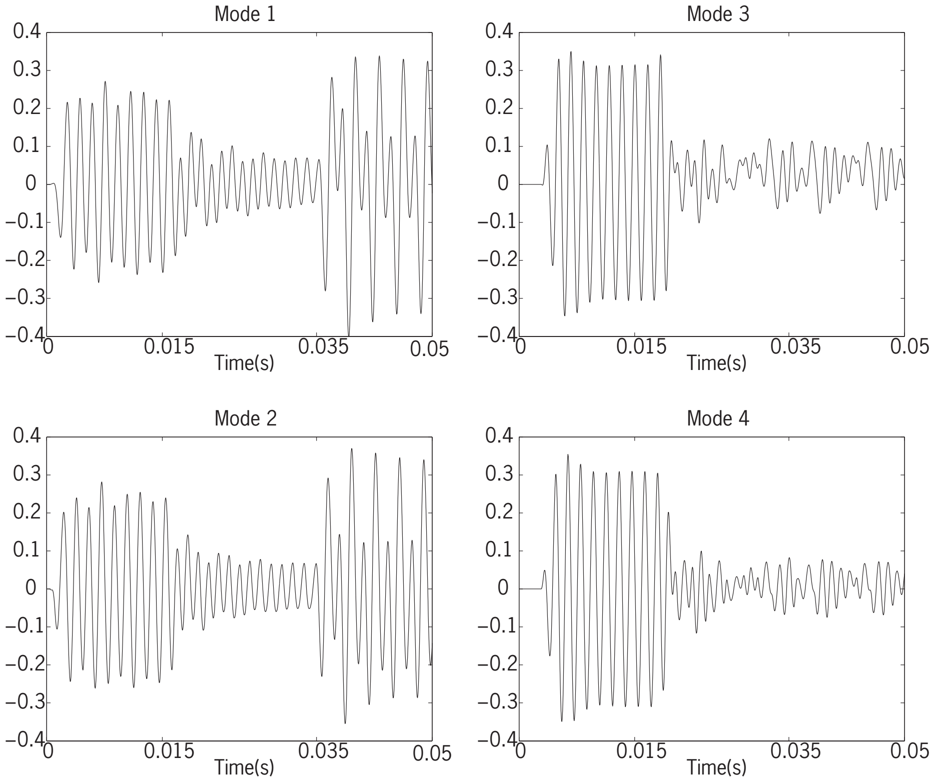

Figure 8: Feedback results using adaptive feedback control. Periodic forcing for 0s $< t <$ 0.015s, closed loop simulation for 0.015s $< t <$ 0.035s, and unforced simulation for $t >$ 0.035s.

gain matrix is of size $n_{in} \times n_{out}$. The time derivative in equation 16 must be approximated numerically, because no analytic solution exists. The fourth order Adams-Bashforth method,

$$\dot{G}_e \simeq \frac{G_{en+1} - G_{en}}{\Delta t}\left(e_{y_n} + \frac{1}{2}\nabla e_{y_{n-1}} + \frac{5}{12}\nabla^2 e_{y_{n-2}} + \frac{3}{8}\nabla^3 e_{y_{n-3}}\right), \tag{17}$$

was utilized to determine the gain matrix derivative. The WNARX model allows for very quick simulation times (approximately two orders of magnitude faster than CFD simulation times), so that closed loop studies can be carried out relatively quickly. The feedback parameters associated with this control strategy are i) POD mode used for feedback, and ii) adaptability weights, which are bounded on the interval [0, 1]. Stability of direct adaptive control for linear systems with extension to nonlinearity and disturbance rejection are proven in (13). Different combinations of modes and their derivatives were fed back along with preconditioned adaptability weights until successful model results were achieved.

After the model feedback studies discussed above, it was determined that the POD mode amplitude a_1 and its time derivative, $\dot{a}_1$, was the appropriate mode choice to regulate the modal amplitudes as shown in Figure 8. The derivative of a_1 was computed by an implicit Euler approximation. Because this can be a poor approximation of the derivative and its susceptibility to noise, a moving average lowpass filter was added to smooth the estimated derivative. Feedback of states a_1 and $\dot{a}_1$ allowed for significant suppression of limit cycle behavior of the mode amplitudes as shown in Figure 8. The idea was that the reduction of the limit cycle behavior in lower frequency modes would also reduce the vortex shedding phenomenon behind the step, and thus reduce the density abberations observed. Note that by controlling mode 1, mode 2 was controlled as well due to the traveling wave character of the shear layer structures. In this simulation, the open-loop forced flow was used as the initial condition for the closed loop simulation to create periodicity in the flow and to improve startup performance of the controller when the loop was closed. Figure 8 shows the time coefficients for the four mode model. Periodic forcing was applied for $t <$ 0.015s, at which point the closed loop control was switched on for a time period of 0.015s $< t <$ 0.035s, when the control is turned off and unforced flow redeveloped for $t >$ 0.035s. As shown in the figure, the controller performs well,

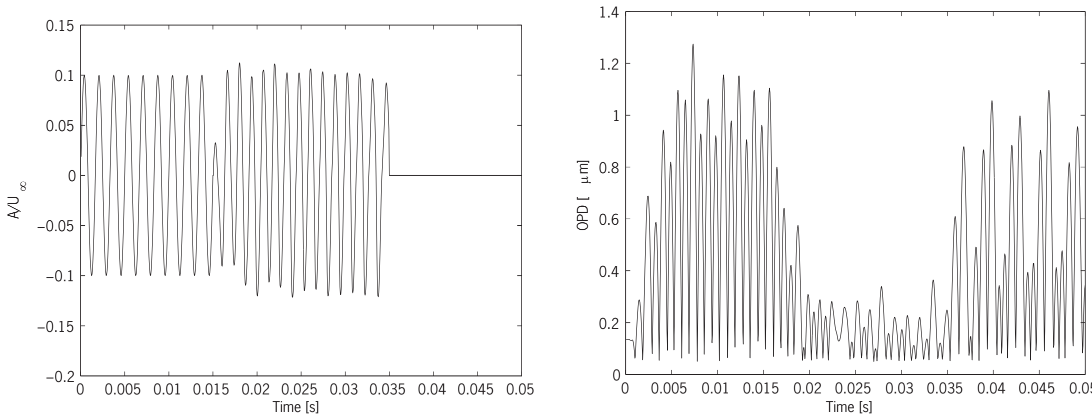

Figure 9: Calculated optical path difference (right) at $x/H = 2$, $y/H = 0$ for the reconstructed flow field of the closed loop simulation. Forcing (left) periodically for $0s < t < 0.015s$, closed loop for $0.015s < t < 0.035s$, and unforced for $t > 0.035s$.

reducing the amplitudes of the time coefficients to approximately 35 per cent of the unforced state.

As a final performance metric, the OPD for a beam passing through this flow field was computed using Equations (1)-(3). For the 2D simulations, the aperture size was $1.5 \leq x/H \leq 2.5$ with unit width. The OPD at the point of interest, $x/H = 2$, is plotted in Figure 9, which shows that the OPD was drastically reduced during the closed loop portion of the simulation, both in comparison to the periodically forced flow and to the unforced flow.

4.2. State Estimation

4.2.1. Sensor Placement

To incorporate the developed adaptive regulator within a CFD simulation, the flow state (i.e. current mode amplitudes) of the flow must be estimated. A surface based estimation scheme was used to determine the current flow state. The main idea is described in (10). The state estimator relates an array of surface mounted sensor signals, defined as $p(x_s,t)$, to the flow state which is modeled by the time coefficients of a POD truncation ($a^f_j(t)$ in equation 7) (Note: the superscript f designates that the parameter is *in the flow,* likewise the s superscript designates that the parameter is *on the surface*). The goal was to incorporate an experimentally feasible number of surface mounted sensors (e.g. pressure transducers) and through mathematical modeling techniques formulate a mapping of sensor signals to the flow state. Having access to the current flow state allows for state feedback flowcontrol. The process of developing the surface based state estimator is described below.

A heuristic approach to sensor placement was used in this study. Locations which are spatially correlated to desired flow features (e.g. vortex shedding, vortex pairing, etc.) are chosen and defined as (x_s) within the numeric simulation. A surface POD analysis,

$$p(x_s,t) \simeq \sum_{p=1}^{k} a_p^s(t)\varphi_p^s(x_s), \tag{18}$$

yields surface POD modes $\varphi^s_p(x_s)$. The locations of the maxima and minima of the surface modes show where the largest variability of the signal occurs; hence, surface POD modes indicate preferred locations for sensors (6). The surface POD analysis allows for the reduction of the number of sensors needed to accurately estimate the surface POD mode amplitudes.

The surface time coefficients (a linear pre-filter) are then computed by solving for $a_p(t)$ in equation (18), given a particular simulation, using

$$a_p^s(t) = p(x_s,t)\varphi_p^{s-1}(x_s). \tag{19}$$

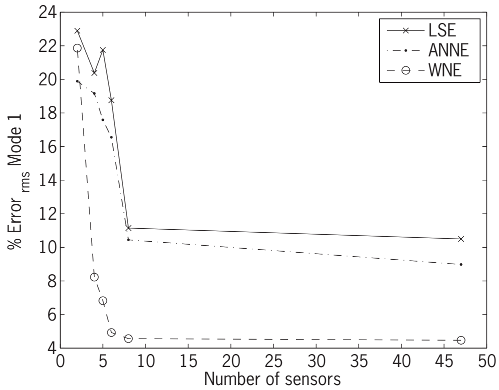

Figure 10: Estimation error for validation case $F_f = 600\text{Hz}$, $A/U_\infty = 0.1$. a) Root mean squared error of mode 1, $a_1(t)$, all estimators.

The matrix $\varphi_p^s(x_s)$ provides the linear subspace, with $dim(a_p^s(x_s)) \leq dim(x_s)$, onto which the sensor signals are projected. The measurement vector is then given by

$$\theta(x_s \mid t) = \begin{bmatrix} p(x_s, t)\varphi_p^{s-1}(x_s) \\ p(x_s, t) \end{bmatrix}, \tag{20}$$

which is mapped to the flow state at a given time. The estimator will yield a model for the POD time coefficients in which the flow state is estimated by the linear or nonlinear mapping of the state vector through the function $\mathbb{G}$,

$$a_j^f(t) \simeq \mathbb{G}(\theta(x_s \mid t)). \tag{21}$$

In the CFD simulation of the backwards facing step, the entire wall behind the step was sampled using 47 sensors. The minima and maxima of surface POD spatial modes allows for optimal downsampling of sensor locations. Figure 10 shows the error in the estimation of mode 1 as a function of the number of sensors, using three typical estimation methods (Linear Stochastic, Artificial Neural Network, and Wavenet estimators). The results indicate that all of the methods rapidly converge to approximately their final performance level with the use of 8 sensors spaced equally between $x/H = 0.25$ and $x/H = 2$.

4.2.2. Wavenet Estimator

Three methods of non-linear model estimation were used to relate the sensor information to flow state estimation. Because the pressure footprint of the flow structures was very small on the surface, linear estimation methods could not be employed. Also, the recirculation zone did add a large amount of noise within the surface pressure measurements. The methods evaluated were linear stochastic estimator (LSE), artificial neural network estimator (ANNE), and wavenet estimator (WNE). Figure 10 shows that the performance of the WNE is superior to LSE and ANNE. The RMS errors for the flow state estimation were on the order of five per cent for this sensor configuration, which was equivalent to the error of the estimation using the full state sensor estimate. More interestingly, the WNE method resulted in only half the error of the other methods. In Figure 11, the errors for all four modes as computed using the WNE estimator are plotted as a function of the number of sensors. The plot indicates that while the error increased somewhat for the higher modes, all modes were converged when using only eight sensors. Figure 11 shows a comparison of the actual time coefficients computed from Equation 7 with the simulated WNE computed from Equation 13 using the eight sensors. The estimator accurately captures the phase, frequency, and amplitude of the flow states for the validation case. With this wavenet estimator, the density field could be reconstructed with an error of less than five per cent of the original flow field using only eight sensors by combining surface POD (Equation 7) and the flow state estimate (Equation 13) within the forcing parameter space.

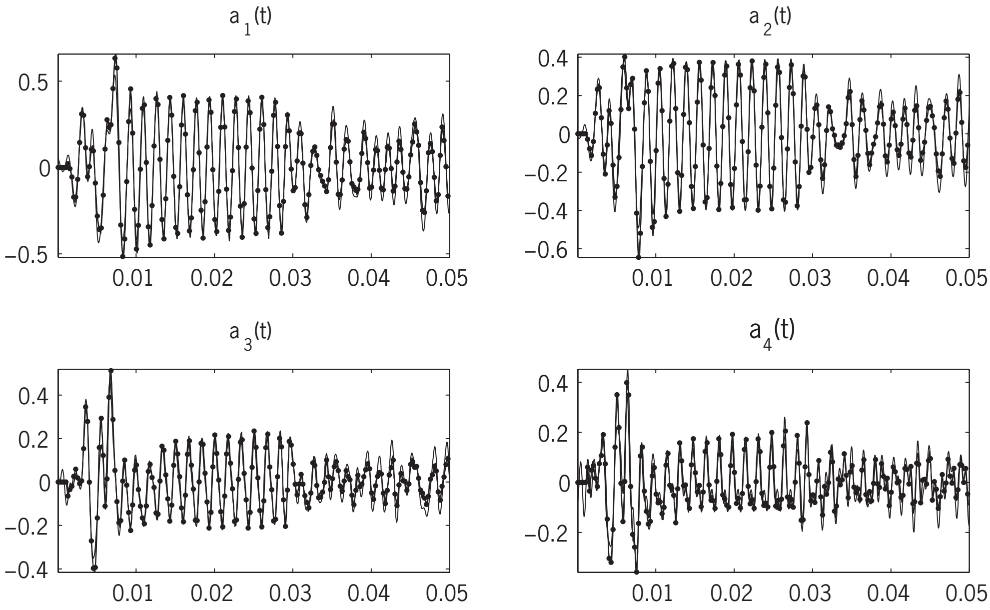

Figure 11: Comparison of first four POD time coefficients for the validation case F_f = 600Hz, A/U_∞ = 0.1. — , CFD results, — · —, WNE with eight sensors. Forcing was active for $t < 0.025s$.

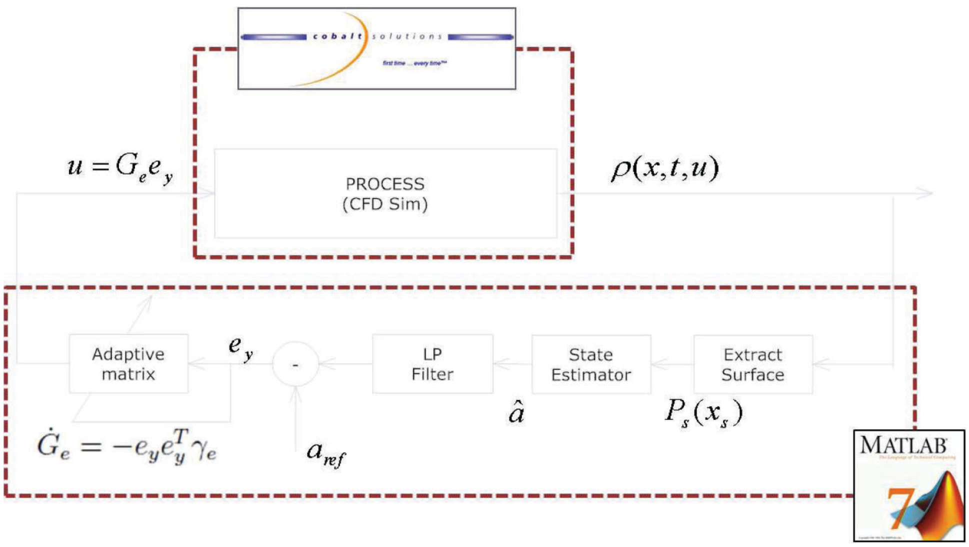

Figure 12: Flowchart of the feedback control development process.

4.3. CFD Feedback Simulation

Once desirable results were achieved with the model in a closed loop simulation, the designed control algorithm with the corresponding feedback mode combination and weights was applied in a closed loop CFD simulation to validate both the WNARX ROM system and the adaptive controller.

Hooks for coupling the COBALT CFD code and Matlab® make sensor information from the CFD simulations available to Matlab® which performs the controller computations. After the actuator output had been determined, it was passed back to the COBALT simulation using the externally controlled blowing and suction boundary conditions in the blowing/suction slot.

The controller in the previous section was directly used in the CFD simulation in conjunction with the state estimator developed in Section 4.1. The feedback controlled simulation proceeded as follows: First, the Cobalt simulation was advanced one time step. The new data at the sensor locations (predetermined, see Section 4.2.1) was then passed to the Matlab® state estimator to estimate the POD mode amplitudes; the estimation was seen to be essentially the same as what the model predicted. These mode amplitude estimates were then input into the control algorithm, whose output was converted to a

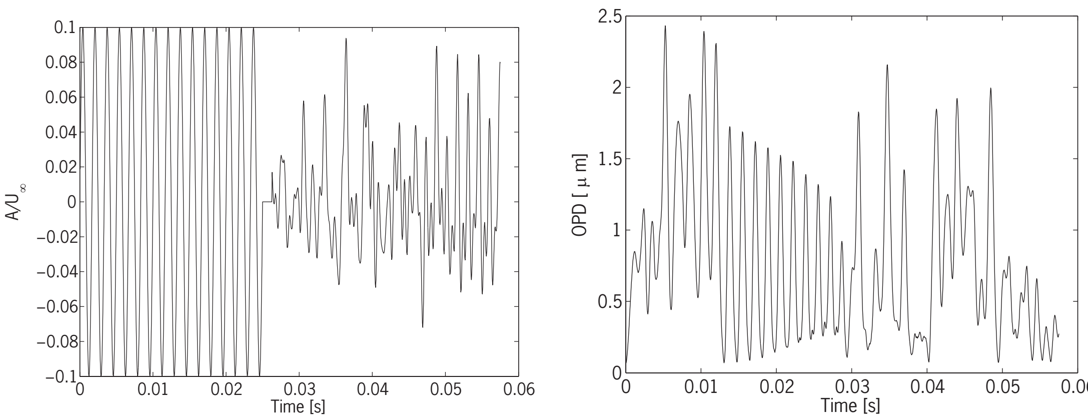

Figure 13: Actuation input (left) shows open loop forcing for $t < 0.025$s and closed loop forcing for $t > 0.025$s. OPD as a function of time (right).CFD results with WNARX controller directly substituted into CFD closed loop simulation.

blowing and suction mass flow rate for the blowing and suction slot. Finally, this information was passed back to COBALT as a new boundary condition value to be used in the subsequent CFD time step.

After completing the feedback controlled simulation, the density field data was used to compute the OPD. The OPD results in Figure 13 show that the controller (active for $t > 0.025$s) reduces the OPD, but the reduction was slower than predicted by the WNARX model. This was most likely due to small discrepancies between the ROM and the CFD simulation results, indicating that the ROM did not quite capture all the intricate nonlinear dynamics of the flow field which were resolved in the CFD simulation, especially during the transient period when the controller is first turned on. As shown in Table 3, the model assumed that modes a_1 and a_2 are decoupled from modes a_3 and a_4, which likely affected the transient dynamics. However, the controller achieved a significant reduction of the mean OPD from $\overline{OPD} \approx 0.8\mu$m to $\overline{OPD} \approx 0.5\mu$m and a reduction in RMS amplitude from $OPD_{rms} \approx 0.7\mu$m to $OPD_{rms} \approx 0.1\mu$m, where

$$OPD_{rms} = \sqrt{\frac{1}{N}\sum_{i=1}^{N} OPD_i^2} \quad \textbf{and} \quad \overline{OPD} = \frac{1}{N}\sum_{i=1}^{N} OPD_i. \tag{22}$$

5. CONCLUSION

The development of a feedback flow control strategy to mitigate the aero-optical aberrations due to the flow behind a backward facing step has been shown. Using unforced and open-loop forced CFD simulations, in which blowing and suction was applied with frequencies between $F_f = 200$Hz and $F_f = 1000$ Hz and amplitudes between $A = 0.25$m/s and $A = 1.5$m/s, a flow state database was developed using Proper Orthogonal Decomposition (POD).

A reduced order model (ROM) was built based on the POD time coefficients and used to develop a wavelet based nonlinear auto-regressive exogenous (ARX) network (WNARX), which described the behavior of the POD time coefficients. This network system allowed for fast simulation time which benefited adaptive feedback controller design, which was the ultimate goal. The network model was able to reproduce training data and validation data to less than one per cent mean squared error.

Based on this model, a controller was developed using the direct adaptive control strategy. The controller was then tested on the newly developed WNARX model of the shear layer. Once satisfactory results were obtained, the control algorithm was applied in the CFD simulations. The controller, solely developed from the model data, resulted in a reduction of the mean OPD of over 35 percent and a reduction in RMS amplitudes of 80 per cent. Feedback control of the shear layer allows for larger reduction in the optical properties when compared to current techniques, such as open loop forcing. Open loop forcing does enforce the periodic vortex shedding of the shear layer and higher frequencies have been shown to reduce the size of the structures and therefore the OPD, but feedback control really allows for the control of the vortex pairing to reduce the structure size over a given location.

REFERENCES

[1] S. Ahuja and C. W. Rowley. Low-Dimensional Models for Feedback Stabilization of Unstable Steady States. In *AIAA Paper* 2008-0553, 2008.

[2] L. Angrisani, P. Daponte, and M. DíApuzzo. A Method Based on Wavelet Networks for the Detection and Classifcation of Transients. *Proceedings of the IEEE Instrumentation and Measurement Technology Conference*, vol. 2,:903–908, 1998.

[3] R. Becker, R. King, R. Petz, and W. Nitsche. Adaptive Closed-Loop Separation Control on a High-Lift Configuration using Extremum Seeking. In *AIAA* 2006-3493, 2006.

[4] G. Berkooz, P. Holmes, and J. L. Lumley. The Proper Orthogonal Decomposition in the Analysis of Turbulent Flows. *Ann. Rev. Fluid Mech.*, 25:539–575, 1993.

[5] J. Chen and D. Bruns. WaveARX Neural Network Development for System Identication Using a Systematic Design Synthesis. *Industrial and Engineering Chemistry Research*, vol. 34:4420–4435, 1995.

[6] K. Cohen, S. Siegel, and T. McLaughlin. Sensor Placement Based on Proper Orthogonal Decomposition Modeling of a Cylinder Wake. In *AIAA Paper* 2003-4259, 2003.

[7] K. Cohen, S. Siegel, J. Seidel, S. Aradag, and T. McLaughlin. Neural Network Estimation of Transient Flow Field Low Dimensional States Using Double Proper Orthogonal Decomposition. 2007.

[8] K. Cohen, S. Siegel, J. Seidel, and T. McLaughlin. Neural Network Estimator for Low-Dimensional Modeling of a Cylinder Wake. In *AIAA Paper* 2006-3491, 2006.

[9] J. A. Cress, S. Gordeyev, E. Jumper, T. T. Ng, and A. B. Cain. Similarities and Differences in Aero-Optical Structure over Cylindrical and Hemispherical Turrets with a Flat Window. In *AIAA Paper* 2007-0326, 2007.

[10] C. P. Fagley, M. J. Balas, J. Seidel, S. Siegel, and T. McLaughlin. Surface Mounted Flow State Estimation of Reduced Order POD Models: Shear Layer. In *AIAA Paper* 2010-7599, 2010.

[11] E. J. Fitzgerald, J. M. Cicchiello, J. P. Siegenthaler, and E. J. Jumper. Optical Characterization of the Notre Dame Compressible Shear-Layer Facility. In *AIAA Paper* 2002-2274, 2002.

[12] E. J. Fitzgerald and E. J. Jumper. The optical distortion mechanism in a nearly incompressible free shear layer. *J. Fluid Mech.*, 512:153–189, 2004.

[13] R. Fuentes and M. Balas. Direct Adaptive Rejection of Persistant Disturbances. *J. Math. Anal. Appl.*, 251:11:28–39, 2000.

[14] J. Gerhard, M. Pastoor, R. King, B. Noack, A. Dillmann, M. Morzynski, and G. Tadmor. Model Based Control of Vortex Shedding using Low-Dimensional Galerkin Models. 2003.

[15] J. J. Gottlieb and C. P. T. Groth. Assessment of Riemann Solvers for Unsteady One- Dimensional Inviscid Flows of Perfect Gases. *J. Comp. Phys.*, 78:437–458, 1988.

[16] M. J. Grismer, W. Z. Strang, R. F. Tomaro, and F. C. Witzemman. Cobalt: A Parallel, Implicit, Unstructured Euler/Navier-Stokes Solver. *Advances in Engineering Software*, 29(3-6):365–373, 1998.

[17] E. Jumper. Recent Advances in the Measurement and Analysis of Dynamic Aero-Optic Interactions (Review Paper). In *AIAA Paper* 1997-2350, 1997.

[18] E. J. Jumper and E. J. Fitzgerald. Recent advances in aero-optics. *Prog. Aero. Sci.*, 37:299–339, 2001.

[19] G. Karypis, K. Schloegel, and V. Kumar. *ParMETIS: Parallel Graph Partitioning and Sparse Matrix Ordering Library Version* 1.0, 1997.

[20] R. King, R. Becker, M. Garwon, and L. Henning. Robust and adaptive closed-loop control of separated shear flows. In *AIAA Paper* 2004-2519, 2004.

[21] M. M. M.M. Polycarpou and S. Weaver. Adaptive Wavelet Control of Nonlinear Systems. *Proceedings of the* 36*th Conference on Decision & Control*, vol. 4:3890–3895, 1997.

[22] J. P. Moeck, M. R. Bothien, C. O. Paschereit, G. Gelbert, and R. King. Two-Parameter Extremum Seeking for Control of Thermoacoustic Instabilities and Characterization of Linear Growth. In *AIAA* 2007-1416, 2007.

[23] A. M. Nightingale, B. Goodwine, M. Lemmon, and E. J. Jumper. "Feedforward" Adaptive-Optic System Identification Analysis for Mitigating Aero-Optic Disturbances. In *AIAA Paper* 2007-4013, 2007.

[24] B. R. Noack, K. Afanasiev, M. Morzynski, G. Tadmor, and F. Thiele. A hierarchy of low-dimensional models for the transient and post-transient cylinder wake. *J. Fluid Mech.*, 497:335–363, 2003.

[25] B. R. Noack, G. Tadmor, and M. Morzynski. Low-dimensional models for feedback flow control. Part I: Empirical Galerkin models. In *AIAA Paper* 2004-2408, 2004.

[26] M. Norgaard, Ravn, O, Poulsen, N. K, Hansen, and L. K. *Neural Networks for Modelling and Control of Dynamic Systems*. Springer Advanced Textbooks in Control and Signal Processing, 2003.

[27] Y. Oussar and G. Dreyfus. Initialization by Selection for Wavelet Network Training. *Neurocomputing*, vol. 34:131–143, 2000.

[28] D. Rempfer. On Low-Dimensional Galerkin Models for Fluid Flow. *Theoret. Comput. Fluid Dyn.*, 14:75–88, 2000.

[29] R. M. Rennie, D. A. Duffin, and E. J. Jumper. Characterization of a Forced Two-Dimensional, Weakly-Compressible Shear Layer. In *AIAA Paper* 2007-4007, 2007.

[30] R. M. Rennie, D. A. Duffin, and E. J. Jumper. Characterization and Aero-Optic Correction of a Forced Two-Dimensional Weakly Compressible Shear Layer. *AIAA J.*, 46(11):2787–2795, 2008.

[31] R. M. Rennie, J. P. Siegenthaler, and E. J. Jumper. Forcing of a Two-Dimensional, Weakly-Compressible Subsonic Free Shear Layer. In *AIAA Paper* 2006-0561, 2006.

[32] C. W. Rowley. Model reduction for fluids, using Balanced Proper Orthogonal Decomposition. *Int. J. on Bifurcation and Chaos*, 15(3):997–1013, 2005.

[33] C. W. Rowley, T. Colonius, and R. M. Murray. Model reduction for compressible flows using POD and Galerkin projection. *Physica D*, 189:115–129, 2004.

[34] J. Seidel, S. Siegel, and T. McLaughlin. Computational Investigation of Aero-Optical Distortions in a Free Shear Layer. In *AIAA Paper* 2009-0362, 2009.

[35] S. Siegel, J. Seidel, C. Fagley, D. Luchtenburg, K. Cohen, and T. McLaughlin. Low-dimensional modelling of a transient cylinder wake using double proper orthogonal decomposition. *J. Fluid Mech.*, 610:1–42, 2008.

[36] J. P. Siegenthaler, E. J. Jumper, and A. Asghar. Preliminary Study in Regularizing the Coherent Structures in a Planar, Weakly-Compressible, Free Shear Layer. In *AIAA Paper* 2003-0680, 2003.

[37] S. Sirisup, G. E. Karniadakis, D. Xiu, and I. G. Kevrekidis. Equation-free/Galerkin-free POD-assisted computation of incompressible flows. *J. Comp. Phys.*, 207:568–587, 2005.

[38] L. Sirovich. Turbulence and the Dynamics of Coherent Structures Part I: Coherent Structures. *Q Appl Math*, 45(3):561–571, 1987.

[39] P. R. Spalart, S. Deck, M. L. Shur, K. D. Squires, M. K. Strelets, and A. Travin. A new version of detached-eddy simulation, resistant to ambiguous grid densities. *Theor. Comput. Fluid Dyn.*, 20:181–195, 2006.

[40] W. Strang, R. Tomaro, and M. Grismer. The Defining Methods of Cobalt60: A Parallel, Implicit, Unstructured Euler/Navier-Stokes Flow Solver. In *AIAA Paper* 1999-0786, 1999.

[41] D. Williams, W. Kerstens, S. Buntain, V. Quach, J. Pfeiffer, R. King, G. Tadmor, and T. Colonius. Closed-Loop Control of a Wing in an Unsteady Flow. In *AIAA Paper* 2010-0358, 2010.

[42] D. J. I. Wittich, D. A. Duffin, E. J. Jumper, A. B. Cain, and E. J. Kerschen. Passive Shear Layer Regularization Experiments in Wind Tunnels and Feed-Forward Adaptive-Optic Correction. In *AIAA Paper* 2009-0358, 2009.

[43] J. Zhang, G. Walter, Y. Miao, and W. Lee. Wavelet Neural Networks for Function Learning. *IEEE Transactions on Signal Processing*, vol. 43, no. 6:1485–1497, 1995.

[44] Q. Zhang and A. Benveniste. Wavelet Networks. *IEEE Transactions on Neural Networks*, 3:889–898, 1992.